NUMERICAL SIMULATION OF INDIVIDUAL BLADE CONTROL

D. Nellessen, G. Britten, J. Ballmann
Lehr- & Forschungsgebiet für Mechanik, RWTH Aachen
D-52056 Aachen

Abstract

The blade-vortex interaction (BVI), which is a major problem of helicopter rotor aerodynamics, causes the typical impulsive noise and vibration. The present study is intended to show that the impulsive noise and also the vibration can be reduced significantly by an individual blade control (IBC). In order to determine an effective control movement, the interaction of a vortex with a moving airfoil has been calculated numerically for several different movements. A two-dimensional model problem which approximates a parallel BVI is considered.
Because of the rotor-blade's elasticity, there has to be a time lag between the introduction of the control movement at the blade's root and the BVI which is most intense close to the blade's tip. Furthermore, the introduced control movement differs from the movement close to the blade's tip due to dispersion.
The calculations are performed using the SOFIA (SOlid-Fluid-InterAction) code. A short validation of the numerical method is included: the head-on collision of a vortex and the eigenvalues of a rotor-blade are calculated and compared with experimental results.

List of symbols

Γ	circulation
M	Mach number
a	speed of sound
$\underset{\sim}{v}$	flow velocity
$\underset{\sim}{\lambda}$	velocity of the grid
$\underset{\sim}{n}$	normal vector
ρ	density
p	pressure
c_p	pressure coefficient
e	total specific energy
c	chord length
Ψ	rotor azimuth angle
Ω	rotational frequency

Indices:

∞	infinity
v	vortex position

Coordinate System:

x,y,z,t inertial reference frame, time

1 Introduction

The interactions of the rotor-blade with the tip vortices of the preceding blades can cause a significant increase in noise and vibration, see Fig. 1. Especially

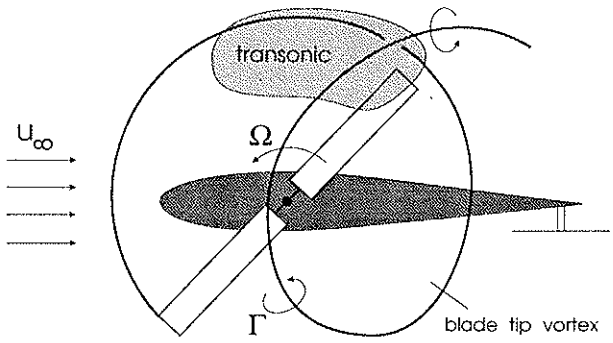

Figure 1: Technical problem

during descent flight conditions at advance ratios of 0.1 - 0.2, BVI is the major source of noise and has a tremendous effect on vibratory airloads because of the small vertical distance between the tip vortex of the previous blade and the rotor-blade itself. In the past many efforts have been made to explain the BVI mechanism. Experiments were carried out by Meier et al [1, 2, 3], Caradonna et al [4, 5], Bershader et al [6, 7], Galbraith et al [8] and van der Wall [9]. Numerical methods were applied by Caradonna et al [10, 11, 12], McCroskey et al [13], Ballmann et al [14, 15, 16, 17, 18] and Schmitz [19]. These investigations show that the fundamental BVI phenomenona are understood fairly well.
During the last two decades active control systems like Higher Harmonic Pitch Control [20] and Individual Blade Control (IBC) [21] have been developed. The control movements of the active control devices are additional pitch motions which are introduced via the pitch horn at the blade's root and influence the angle of attack in an appropriate way to minimize vibration and BVI noise. When applying the active control devices the question arises: which active control movement (amplitude and time history) leads to a reduction of noise and vibration?
A major problem arises from the fact that the rotor-blade is elastic and that its torsional wave speed is only about 500 m/s (by comparison: the torsional wave speed in steel is approximately 3000 m/s). Du-

ring a parallel BVI which takes place within about 10 degrees azimuth (5 milliseconds) a torsional wave can travel only about 2.5 m (less than the rotor's radius). Thus, there has to be a time lag between the introduction of the control movement at the blade's root and the BVI which is most intense close to the blade's tip. Furthermore, the movement at the blade's tip differs from the introduced movement at the blade's root due to dispersion.

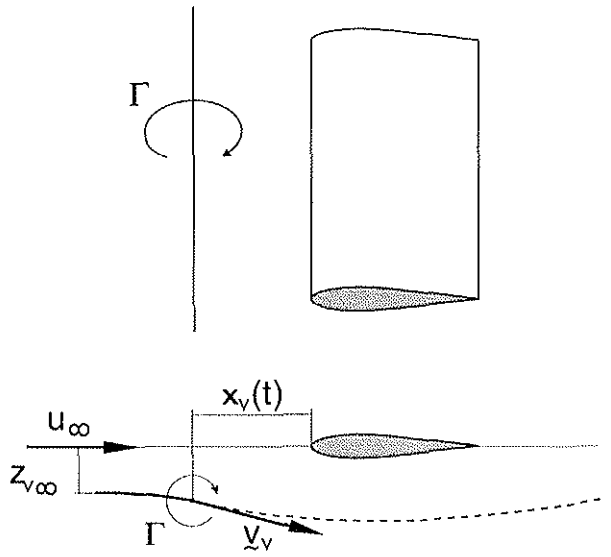

Figure 2: Model problem

First of all, we investigated the interaction of a vortex with an elastic rotor-blade. The rotor-blade's material properties (distribution of stiffness and mass, location of the torsional center, bending center and center of gravity) were varied in order to find out if the fundamental BVI phenomena can be influenced by the blade's elastic motion. Although this seems to be possible, the necessary material properties cannot be realized in a realistic rotor-blade [22]; therefore, active control devices are required. The major task of the present study is to show that the BVI noise and vibration can be reduced by IBC. For this purpose the two-dimensional model problem of a parallel BVI is considered, see Fig. 2. Numerical simulations of the interaction of a vortex with a moving airfoil were carried out, where the movements of the airfoil were given solely functions of time. An effective movement has been identified and will be discussed in detail later. At this point two questions arise: 1) How should the rotor-blade's root move in order to get the previously determined movement at a cross-section close to the blade's tip where the BVI is most intense? 2) When should this control movement be introduced at the rotor-blade's root? A satisfying answer to these questions cannot be given yet, since it requires an inverse numerical method. Therefore the movement close to the blade's tip has been calculated for several control movements introduced at the blade's root - taking into account the static and dynamic coupling of the torsional and bending modes but neglecting the aeroelastic coupling.

The numerical investigations have been performed using the SOFIA code (SOlid-Fluid-InterAction) [23], which was developed to model and analyze aeroelastic phenomena. A very brief description of the two modules - INFLEX for the flow analysis and ODISA (One-Dimensional Structural Analysis) for the structural analysis - that are required to accomplish BVI computations for rigid and especially elastic rotor-blades is given. The well-known code INFLEX was developed by Eberle and Brenneis [24]. A comprehensive evaluation was carried out based on the Two- and Three-dimensional AGARD Standard-Configurations [25].

2 Physical Model

Flowfield

Unsteady flow phenomena like strong acoustic waves and moving shock waves occur on the advancing side of the rotor where the intensive BVI takes place at azimuthal angles between 20 and 70 degrees. As the flow is attached in this regime, viscosity effects are neglected. For the computation of the unsteady, compressible flow about the elastic rotor-blade the Euler equations

$$\begin{aligned}
\frac{\delta}{\delta t}\int_{V(t)} \rho dV &+ \int_{\partial V(t)} \rho(\underset{\sim}{v}-\underset{\sim}{\lambda})\cdot\underset{\sim}{n}dS = 0\,,\\
\frac{\delta}{\delta t}\int_{V(t)} \rho\underset{\sim}{v}dV &+ \int_{\partial V(t)} [\rho\underset{\sim}{v}\circ(\underset{\sim}{v}-\underset{\sim}{\lambda})]\cdot\underset{\sim}{n}dS\\
&= -\int_{\partial V(t)} p\,\underset{\sim}{n}dS\,,\\
\frac{\delta}{\delta t}\int_{V(t)} e dV &+ \int_{\partial V(t)} e(\underset{\sim}{v}-\underset{\sim}{\lambda})\cdot\underset{\sim}{n}dS\\
&= -\int_{\partial V(t)} p(\underset{\sim}{v}\cdot\underset{\sim}{n})dS\,.
\end{aligned}$$

are solved for time-dependent non material balance volumes. $\delta(\ldots)/\delta t$ is the time derivative in a balance volume fixed frame. In the above equations the velocity of the surface of the balance volume is denoted by $\underset{\sim}{\lambda}$. This velocity takes the rotation of the rotor-blade, the cyclic pitch variation as well as the blade's deformation into account. The gas is assumed to be thermally and calorically perfect.

Deformation of the Rotor-Blade

As the aspect ratio of a rotor-blade is high it is modelled by a Timoshenko beam with generally non-coinciding centerlines of mass, bending and torsion. Six functions of the spatial co-ordinate along the beam axis and the time are introduced which represent the three translational and the three rotational degrees

of freedom of each cross-section and determine the location of the beam in space and time. For many engineering purposes the number of independent functions is reduced by neglecting the shear deformation; the bending angles and the corresponding translational degrees of freedom are then coupled by kinematic constraints. Furthermore, in many applications the rotatory inertia of the bending modes are neglected; this results in the well-known Euler and Bernoulli beam theory [26]. Although the results of this model do not differ very much from results with the Timoshenko approximation in case of static problems of slender beams, computations of dynamical problems may show remarkable discrepancies, as the Euler-Bernoulli beam theory leads to a phase velocity which increases with decreasing wavelength out of bound. Moreover the group velocity with which the energy is transported is twice as fast as the phase velocity (anomalous dispersion).

The calculation of the structural deformation is performed in the rotating frame. Assuming the rotating rotor-blade with constant angle of attack as the reference configuration, the deformations in the rotating frame are small and the governing equations can be linearized. The centrifugal stiffening effect is taken into account in the usual way [27, 28]: The axial force is divided into two parts. One part depends on the longitudinal deformation whereas the other part is independent of the deformation and can be calculated from the axial force equilibrium equation for an unloaded rotating beam by spatial integration. This second part leads to an additional term in the variational equation or in the partial differential equation for free vibration of a rotating beam out of its plane of rotation. A detailed description can be found in [23].

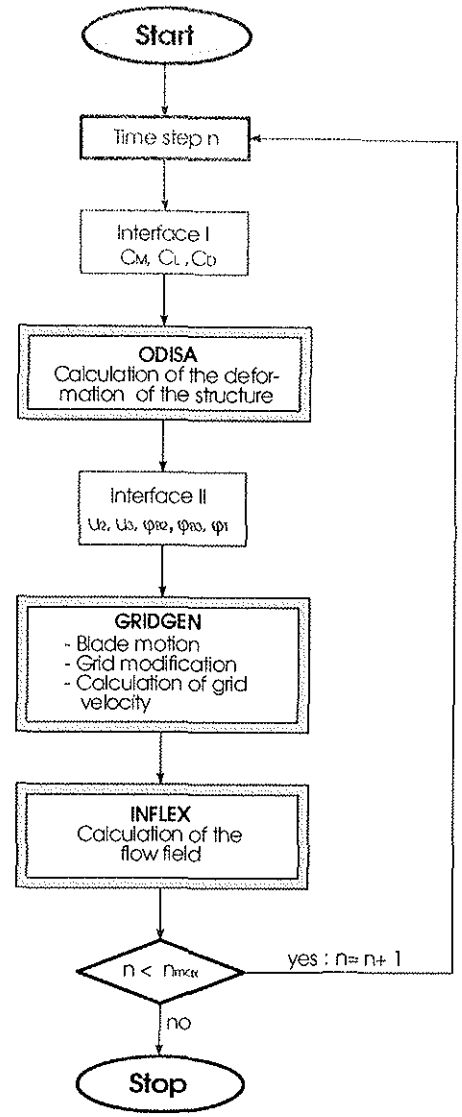

Figure 3: Solution strategy

3 Solution Strategy

Concerning aeroelastic applications, the equations describing the flowfield and the structural deformation are integrated with respect to time simultaneously. The flow-chart in Fig. 3 illustrates the solution strategy. The main time loop consists of three fundamental parts: ODISA calculates the deformation of the rotor-blade, which depends on the current airload. The points at the inner boundary of the numerical grid of the flow solver representing the surface of the rotor-blade are moved according to the calculated deformation of the rotor-blade and the cyclic pitch variation. This is done by GRIDGEN (GRID GENerator). All grid points are rotated about the helicopter's main rotor axis. Finally, the grid points within the flowfield are rearranged by GRIDGEN. In the third part of SOFIA the flowfield is calculated for the actual configuration. This means that the flow velocity perpendicular to the moving rotor-blade's surface has to be zero consistently.

Numerical Method: Calculation of the Flowfield

For the numerical integration of the strong conservation form of the Euler equations an implicit relaxation scheme is used. The unfactored Euler equations are solved by applying a Newton method. Relaxation is performed with a point Gauss-Seidel algorithm. The combination of a Newton method with a point Gauss-Seidel algorithm leads to a robust numerical scheme. Concerning the resolution of pressure and shock waves a characteristic variable splitting technique is employed.

Numerical Method: Grid-Generation

An elliptic grid generator is employed to calculate the grid at each time step. A system of 3 elliptic differential equations (DEs) of second order (Poisson- and Laplace- equation) is solved. The DEs are approximated by central difference schemes. The resulting linear equation system is solved iteratively by applying

a Gauss- Seidel- algorithm. As each grid deviates only slightly from the grid at the preceding time step, only few iterations are necessary.

Numerical Method: Calculation of the Structural Deformation

A finite element method has been developed for the Timoshenko beam: a system of ordinary differential equations (ODEs) which is second order in time to determine the generalized deflections is derived by applying Hamilton's principle and the method of Ritz/Kantorowitsch. Discretization is done by isoparametric, two-noded elements. Shear locking is avoided by a reduced integration scheme [29]. The set of ODEs is integrated by Newmark's method, where the resulting linear system of equations is solved directly with a LU-decomposition. The external forces are assumed to vary linearly during a time-step.

4 Results

Mechanism of BVI and Validation

The comparison of the predicted pressure wave propagation phenomena during BVI with experimental results is a good accuracy test for a CFD-method. Caradonna's experiment concerning parallel and oblique BVI obtained in NASA Ames' 80 by 120 foot Wind Tunnel is ideal for such a validation. An extensive description of the test stand and the experimental results can be found in [5]. Fig. 4 illustrates the experimental

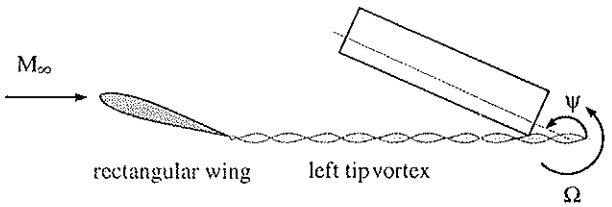

Figure 4: Experimental configuration

configuration. The vortex is generated separately by a wing tip placed upstream of the rotor. This makes an independent control of the interaction parameters like vertical miss distance, vortex strength etc. possible. The two-bladed rotor itself operates at zero thrust to avoid any influence of the rotor's wake. The head-on collision (no vertical distance between vortex and rotor-blade) for a Mach number of 0.63 and a dimensionless vorticity of 0.25 has been calculated. This corresponds to the flow conditions at a radial position of $r/R = 0.9$ and a tip Mach number of 0.7 in Caradonna's experiment. The computation is initiated by introducing a Lamb-Oseen vortex four chord lengths in front of the airfoil's leading edge. Figure 5 shows the time histories of the pressure coefficient at different positions on the lower side during the parallel BVI. The comparison with the experimental results

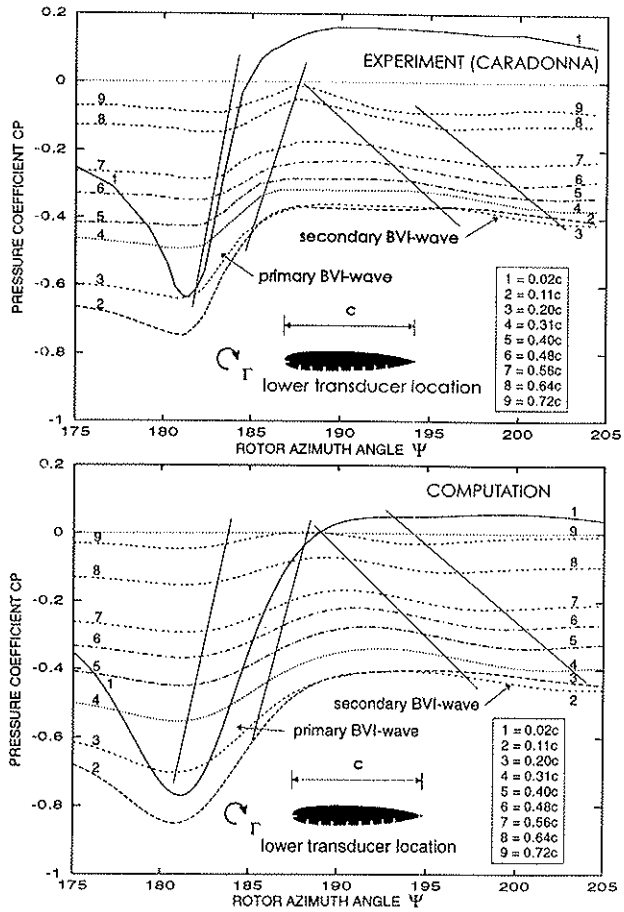

Figure 5: Comparison of measured and computated pressure coefficient at the lower side during BVI ($M_\infty = 0.63$, $\Gamma = 0.25$, $z_v = 0.$, NACA0012)

show that all the important flow features, especially the propagative and convective events are captured well by the numerical method. The most significant pressure variations are observed at positions x/c=0.02 close to the leading edge: when the vortex approaches the leading edge, the stagnation point moves first to the upper surface causing a pressure increase there. The stagnation point moves then very fast to the lower side when the vortex passes the leading edge. This causes decreasing pressure values on the upper side and results in a separation of a region of high pressure, which propagates upstream above the airfoil's axis. This wave is referred to as the **compressibility wave** [3] and its development is a result of the so-called **leading edge effects**. The movement of the stagnation point and the development of the compressibility wave can be recognized in Fig. 6 where the pressure field is depicted for a sequence of time steps. The movement of the stagnation point onto the upper side has another consequence: a negative angle of attack is induced and the flow on the lower side is accelerated. This causes decreasing pressure values on the lower side, see Fig. 5, at $\Psi \approx 180°$. When the stagnation point jumps to the lower side because of the passing vortex, a positive angle of attack is suddenly

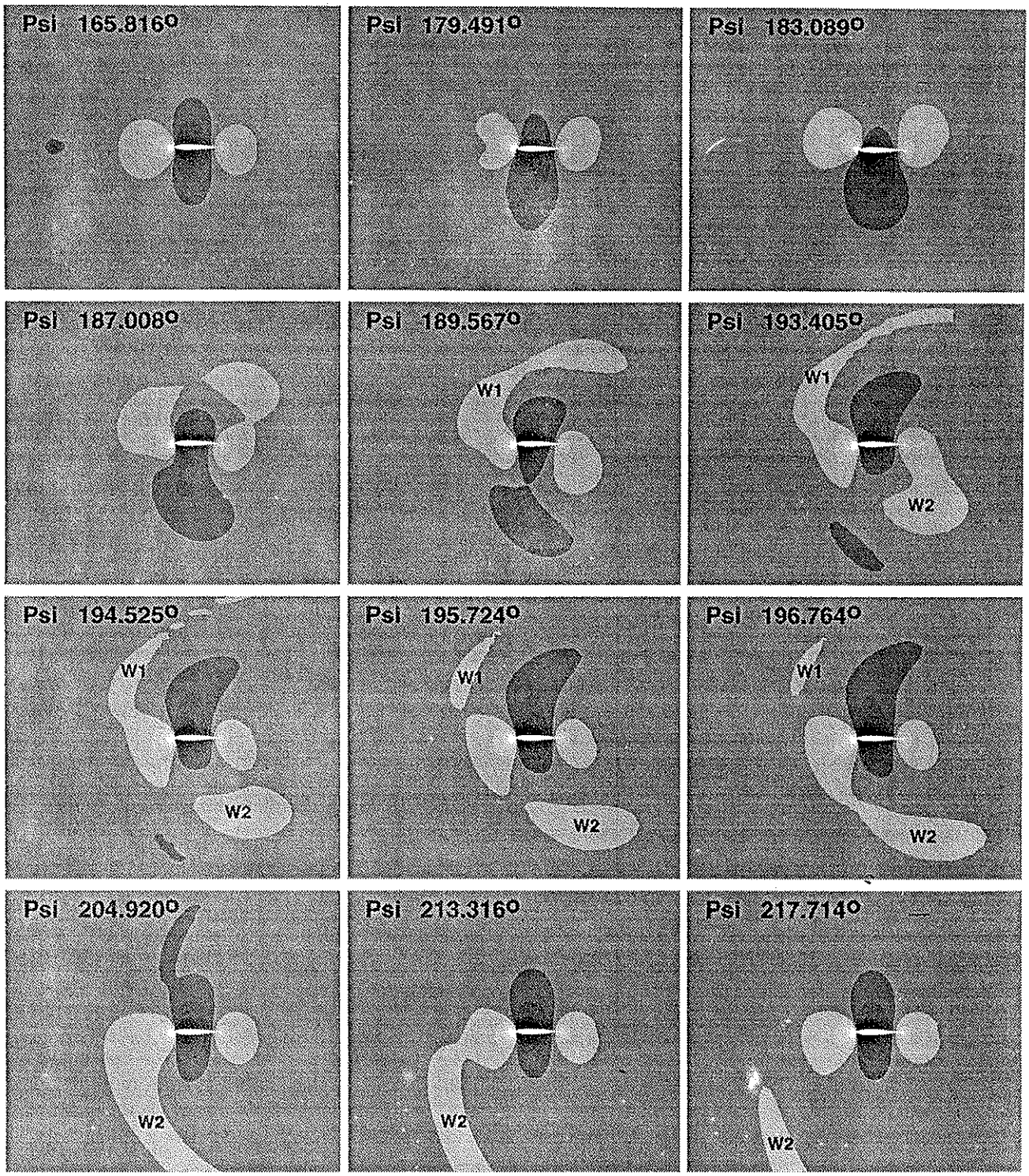

Figure 6: Pressure contours for a sequence of time steps during BVI for the rigid case ($M_\infty = 0.63$, $\Gamma = 0.25$, $z_v = 0.$, NACA0012)

induced and a wave propagates downstream with a speed of the local flow velocity plus the local speed of sound, see Fig. 5 at $\Psi \approx 185°$ ("primary BVI-wave"). Fig. 7 shows the history of the Mach number during the BVI for the complete lower side of the airfoil in a three-dimensional plot. The downstream travelling primary wave is obvious. When approaching the airfoil the vortex and the airfoil act as some kind of a convergent nozzle, where the flow is accelerated. This **nozzle effect** is pronounced in case of no head-on collision [18] and depends strongly on the free flow Mach number and the strength of the vortex:

- In the case of head-on collision no supersonic pocket bounded with a shock wave has been observed.
- If the relative free flow Mach number and the strength of the vortex exceed a certain level, the reduction in pressure may be strong enough to produce a transient supersonic pocket which is bounded downstream by a shock wave, see Fig. 19 ($t = 16.3ms$ in the figure) and Fig. 8. When the vortex passes the shock wave, the acceleration of the flow is reversed and the region of overexpansion on the lower side collapses. The shock wave moves upstream diminishing continuously and leaving the leading edge as a pressure wave in a downwards inclined direction. This wave is often called the **transonic wave**.
- For a high relative free flow Mach number the steady state flow about the airfoil can have a supersonic pocket which is bounded by a shock wave. Then the nozzle effect leads to a pulsation of the shock wave.

The first two cases seem to be most important for realistic flight conditions.
The three-dimensional plot of the history of the Mach number for the whole lower side, Fig. 7, shows a second wave which starts at the trailing edge and propagates upstream with the local speed of sound minus the local flow velocity. This corresponds to Caradonna's results, see Fig. 5 and for more details [5]. In this reference two possible reasons for that secondary wave, named **Kutta wave**, are discussed: it can either be in response to the primary wave or to the passing vortex. In accordance with [5] we believe also that the latter wave is a response to the primary wave. This **trailing edge wave** was first detected numerically by Kocaaydin and Ballmann [14] and it was observed in Göttingen's shock tube by Meier et al [3]. In Fig. 10 the pressure field is depicted for a sequence of time steps; one can see very clearly that a region of high pressure is separated at the trailing edge ($\Psi = 194.525°$ in the figure). This upstream propagating region of high pressure arises also in case of a higher Mach number and a stronger vortex, see Fig. 19 ($t = 20.8ms$ in the figure).

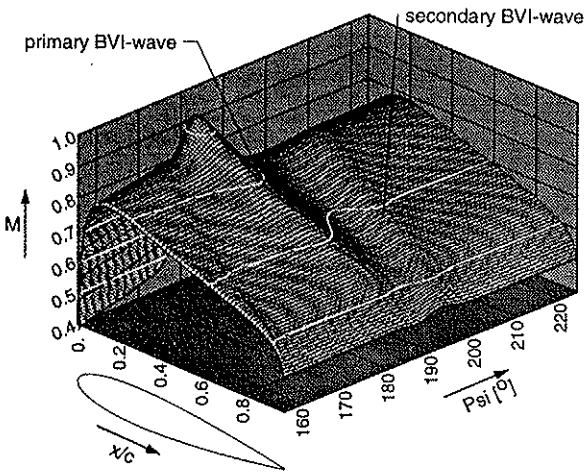

Figure 7: Mach number at lower side during BVI ($M_\infty = 0.63$, $\Gamma = 0.25$, $z_v = 0.$, NACA0012)

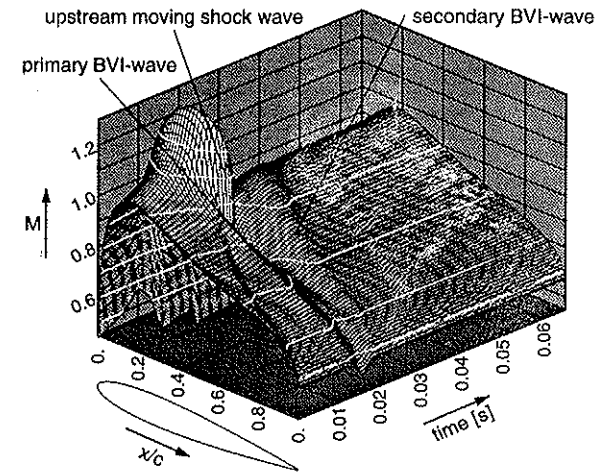

Figure 8: Mach number at lower side during BVI ($M_\infty = 0.73$, $\Gamma = 0.4$, $z_v = -0.26$, NACA0012)

Due to the high resolution of the H-type grid the wave propagation is predictable up to five chords ahead of the airfoil. Figures 9, 10 and 11 show time histories of the pressure coefficient at nine different observer positions depicted in the corresponding figures. In Fig. 9 three observer locations along a ray at 30 degrees below the airfoil axis are shown. The first peak stems from the vortex itself which is even more obvious in Fig. 10 where the vortex core passes through the observer points 3, 2 and 1 respectively. In figure Fig. 9 one detects three major waves which travel upstream. The first wave (**w1**) is the compressibility wave which occurs due to the sudden motion of the stagnation point when the vortex passes the leading edge (see above). The second wave (**w2**) or transonic wave can hardly be recognized at the first observer location but shows up significantly at position 2 and 3; this second wave can be attributed to the high pressure region which has been separated at the trailing edge. The final third wave phenomenon (**w3**) is the trailing edge

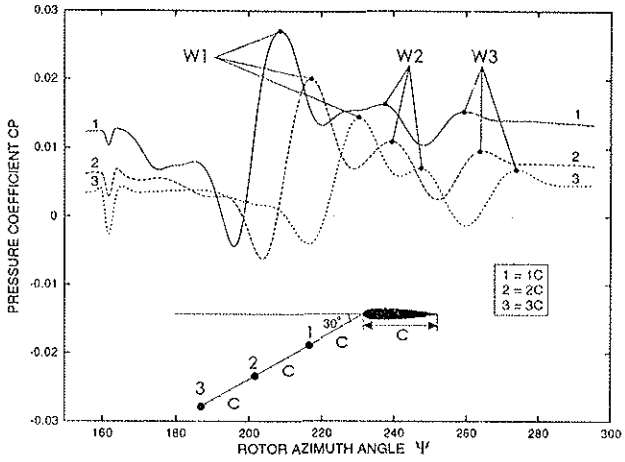

Figure 9: Pressure variations due to BVI at three different observer locations below the airfoil ($M_\infty = 0.63$, $\Gamma = 0.25$, $z_v = 0.$, NACA0012)

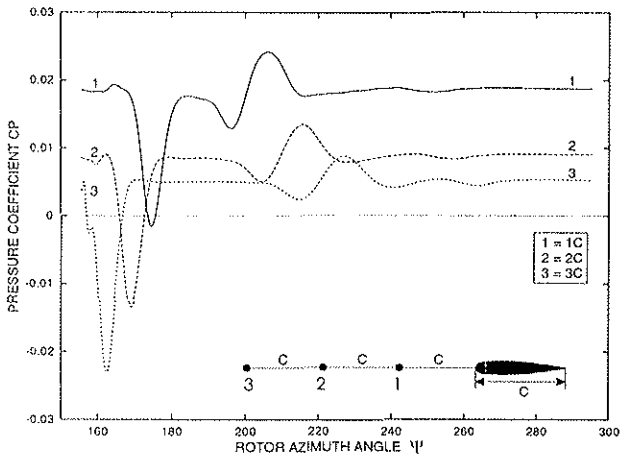

Figure 10: Pressure variations due to BVI at three different observer locations in front of the leading edge ($M_\infty = 0.63$, $\Gamma = 0.25$, $z_v = 0.$, NACA0012)

wave which can be observed in Fig. 11 as well.
Here the following problem arises: In Fig. 9 three major waves can be detected (denoted w1, w2 and w3), whereas in Fig. 5 and 7 only two BVI-waves traveling along the airfoil are visible (termed "primary BVI-wave" and "secondary BVI-wave"). As mentioned earlier, the first wave (w1) in Fig. 9 occurs due to the sudden motion of the stagnation point and is not a result either of the "primary BVI-wave" or of the "secondary BVI-wave" visible in Fig. 5 and 7, respectively. In Fig. 7 depicting the pressure field for a sequence of time steps, one can see that the wave w2 originates from a high pressure region which has been separated by the vortex at the trailing edge. This has been a fundamental insight for the development of an effective control movement and will be discussed in the chapter after next. The third wave (w3) in Fig. 9 originates from the upstream moving trailing edge wave denoted "secondary BVI-wave" in Fig. 5.
The amplitudes of the three waves w1, w2 and w3 in Fig. 5 depend strongly on the free flow Mach number

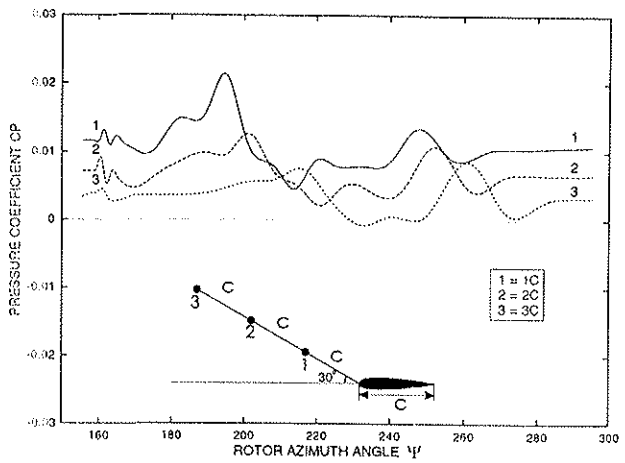

Figure 11: Pressure variations due to BVI at three different observer locations above the airfoil ($M_\infty = 0.63$, $\Gamma = 0.25$, $z_v = 0.$, NACA0012)

and the strength of the vortex. The second wave (w2) is much stronger compared to the other two, if the free flow Mach number and the strength of the vortex are high enough to produce temporarily a downstreem closed shock-bounded supersonic pocket at the lower side of the airfoil. This can be seen in Fig. 21. The figure shows the time histories of the pressure coefficient during BVI at two different observer positions for $M_\infty = 0.73$, $\Gamma = 0.4$ and a vertical miss distance of $z_v = -0.26$. In the rigid case the second wave (w2) predominates. (The results concerning the IBC-case will be discussed in the chapter after next.) Fig. 8 shows the history of the Mach number for the whole lower side in a three-dimensional plot. The primary and the secondary wave and also the supersonic pocket, which exists temporarily, can be seen. These wave phenomena are even more obvious in Fig. 12. This figure presents the isolines of the history of the Mach number for the whole lower side in a plan view. The corresponding results for the computation of Caradonna's experiment are shown in Fig. 13. The upstream moving shock wave, which does not occur in the computation of Caradonna's experiment, leads to a strong wave w2 below the airfoil; therefore the wave w2 is sometimes referred to as the transonic wave. But obviously the upstream moving shock wave is not required for the occurrence of the wave w2, since this wave occurs in both cases discussed here.

For the validation of the structural model and the finite element method the eigenfrequencies of the first modes of a model rotor have been calculated. This model rotor was built and tested at NASA [30]. Fig. 14 shows the eigenfrequencies as a function of the rotor's frequency calculated by ODISA. In Fig. 15 the corresponding eigenfrequencies taken from [30] are given. The last figure contains calculated and measured values.

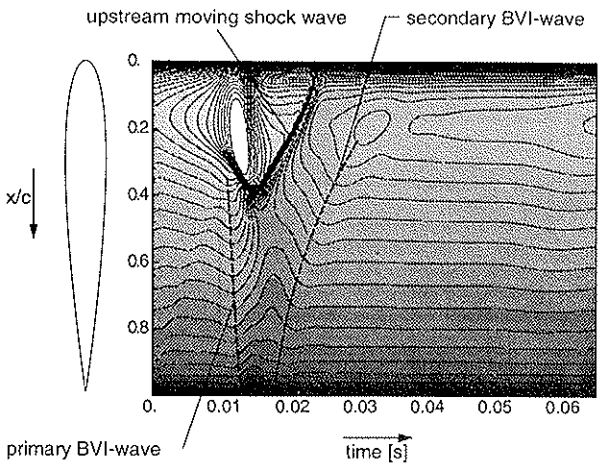

Figure 12: Isolines of the history of the Mach number at lower side during BVI ($M_\infty = 0.73$, $\Gamma = 0.4$, $z_v = -0.26$, NACA0012)

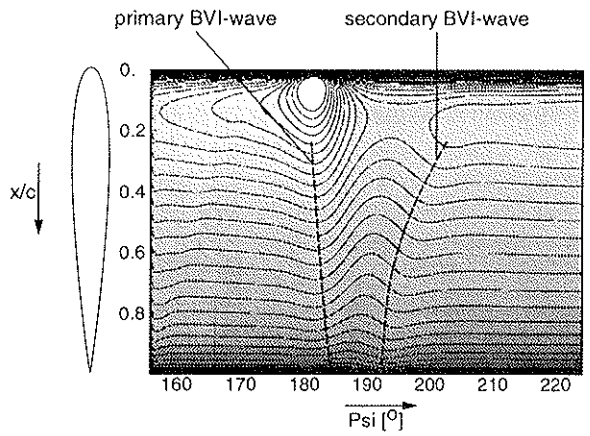

Figure 13: Isolines of the history of the Mach number at lower side during BVI ($M_\infty = 0.63$, $\Gamma = 0.25$, $z_v = 0.$, NACA0012)

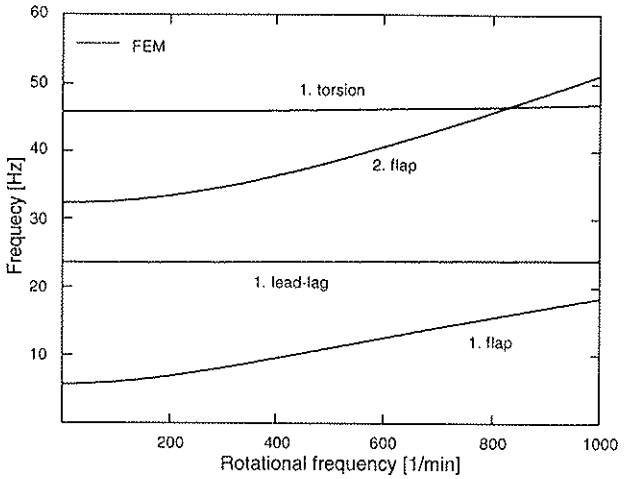

Figure 14: Calculated eigenfrequencies of a model rotor-blade versus the rotor's rotational frequency

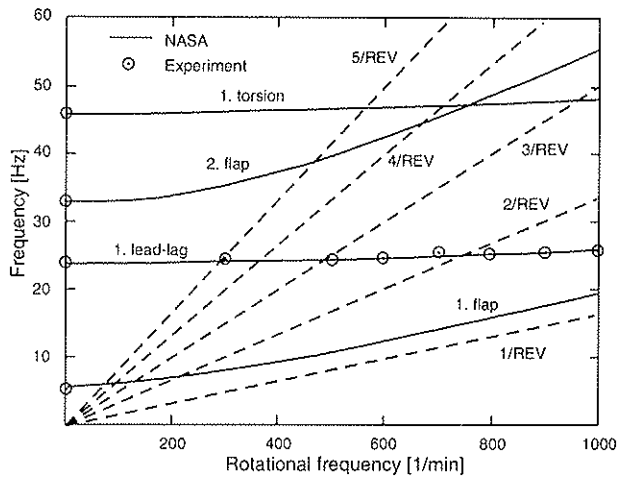

Figure 15: Eigenfrequencies of a model rotor-blade versus the rotor's rotational frequency, taken from [30]

Noise Reduction by the Blade's Elastic Motion

The rotorblade's material properties (stiffness, mass and the locations of the torsional center and the center of gravity) were varied in order to analyse wether the fundamental BVI phenomena can be influenced by the blade's elastic motion. We considered the two-dimensional model problem of a parallel BVI, where the airfoil has only a rotatory degree of freedom. The Fig. 16 shows a comparison of the upstream propagating waves, which occur during the interaction of a vortex with a rigid and with an elastically suspended airfoil ($M_\infty = 0.73$, $\Gamma = 0.4$, $z_v = -0.26$). The compressibility wave (w1) is much weaker in case of the elastically suspended airfoil. The Fig. 17 presents the time history of the angle of attack of the elastically suspended airfoil during the BVI. As described in the previous chapter for the rigid case the passing vortex causes the stagnation point to move first on the upper and then on the lower side of the airfoil. Thereby a negative angle of attack is induced by the vortex until the vortex approaches the leading edge. Then having passed the leading edge the vortex induces a positive angle of attack. In the elastic case the rotatory deflection compensates partly the angle of attack induced by the vortex and the displacement of the stagnation point relative to the airfoil is reduced. This effect is responsible for the reduction of the compressibility wave (w1). However from an aeroacoustic point of view the reduction of the wave w2 - or transonic wave - is more important, since this wave is radiated in a downward direction.

Noise Reduction by IBC

Approaching the leading edge the vortex induces a negative angle of attack; as a result the flow on the lower side is accelerated and a shock-closed supersonic pocket is produced (for $M_\infty = 0.75$, $\Gamma = 0.4$, $z_v =$

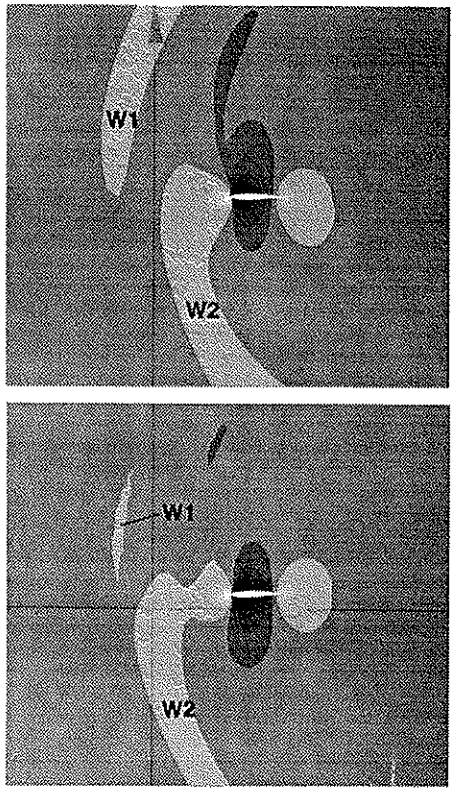

Figure 16: Calculated pressure distribution at $t = 34.0ms$ during BVI for the rigid and elastic case ($M_\infty = 0.73$, $\Gamma = 0.4$, $z_v = -0.26$, NACA0012)

-0.26). First we looked for a control movement that would reduce the vortex-induced acceleration of the flow on the lower side in order to avoid the appearence of the shock wave. Therefore we choosed a control movement similar to the elastic motion, discussed in the previous chapter, but with a higher maximum angle of attack in order to improve the compensation of the vortex-induced angle of attack. In fact this led to the desired reduction of the acceleration of the flow and to a further reduction of the compressibility wave (w1). However, a significant reduction of the transonic wave (w2) was not obtained.

Then we searched for a control movement that would reduce the region of high pressure that is separated by the vortex at the trailing edge. A very important parameter concerning this separation is the distance between the trailing edge and the passing vortex. To reduce this distance we choosed a control movement such that the angle of attack is negative when the vortex passes the trailing edge. The best results were obtained when the minimum angle of attack was attained before the vortex approached the trailing edge. Fig. 19 and Fig. 20 depict the pressure field for a sequence of time steps during BVI with (**IBC-case**) and without (**rigid case**) the control movement ($M_\infty = 0.75$, $\Gamma = 0.4$, $z_v = -0.26$). As can be seen, the control movement leads to a significant reduction of the transonic wave (w2). The time history of the

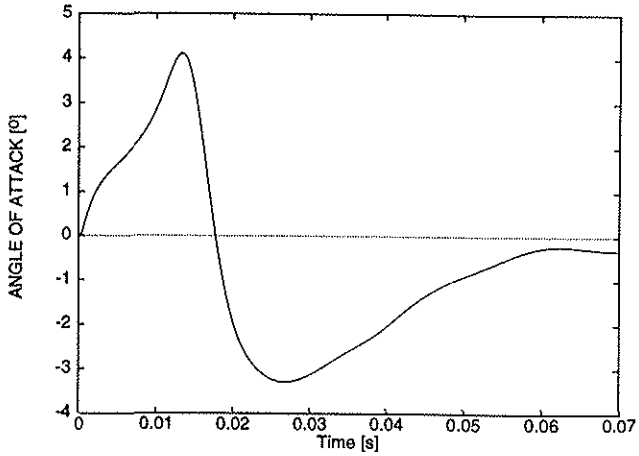

Figure 17: Time history of the angle of attack during BVI in case of an elastically suspended airfoil ($M_\infty = 0.73$, $\Gamma = 0.4$, $z_v = -0.26$, NACA0012)

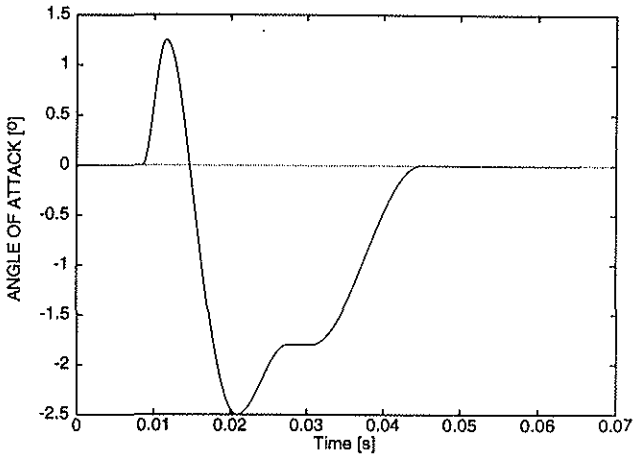

Figure 18: Time history of the angle of attack during BVI in the IBC-case ($M_\infty = 0.73$, $\Gamma = 0.4$, $z_v = -0.26$, NACA0012)

angle of attack is shown in Fig. 18. In the figure Fig. 21 the time history of the pressure coefficient at two observer points below the airfoil are compared for the rigid case and the IBC-case. The tremendous reduction of the transonic wave (w2) is obvious. Fig. 22 presents a three-dimensional plot of the history of the Mach number for the whole lower side and Fig. 23 shows the isolines of the history of the Mach number in a plan view. The corresponding figures for the rigid case are Fig. 8 and Fig. 12, respectively.

5 Conlusions and Perspectives

The time dependent flow field about a rotor–blade during BVI has been simulated for a 2D model using the Euler equations. The comparison with experimental results shows 2D–model is suitable to describe the pressure wave generation and propagation phenomena during BVI. Calculations performed for elastically suspended rotor–blade segments have revealed that BVI–noise and vibrations can be reduced. The-

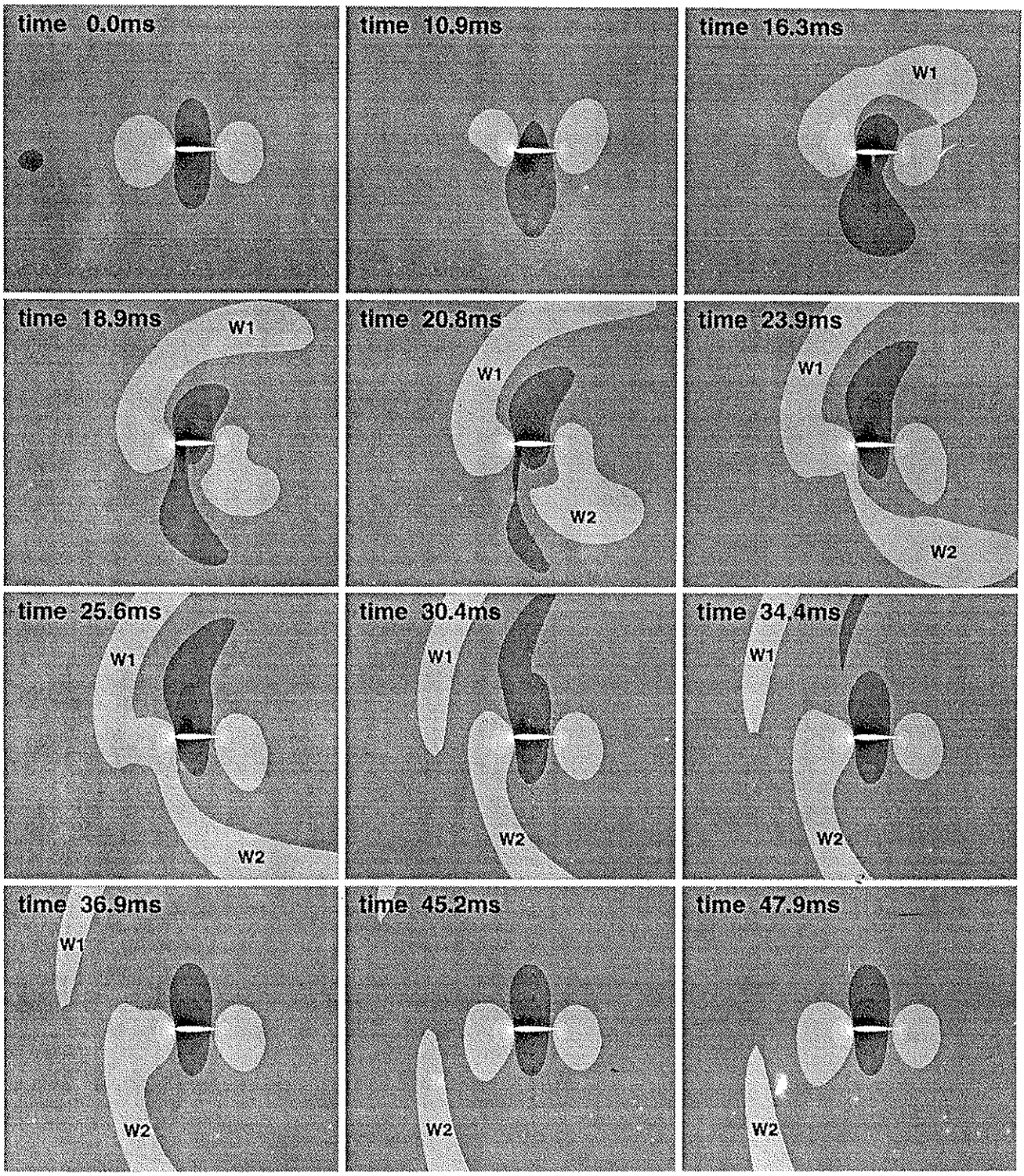

Figure 19: Pressure contours for a sequence of time steps during BVI for the rigid case ($M_\infty = 0.73$, $\Gamma = 0.4$, $z_v = -0.26$, NACA0012)

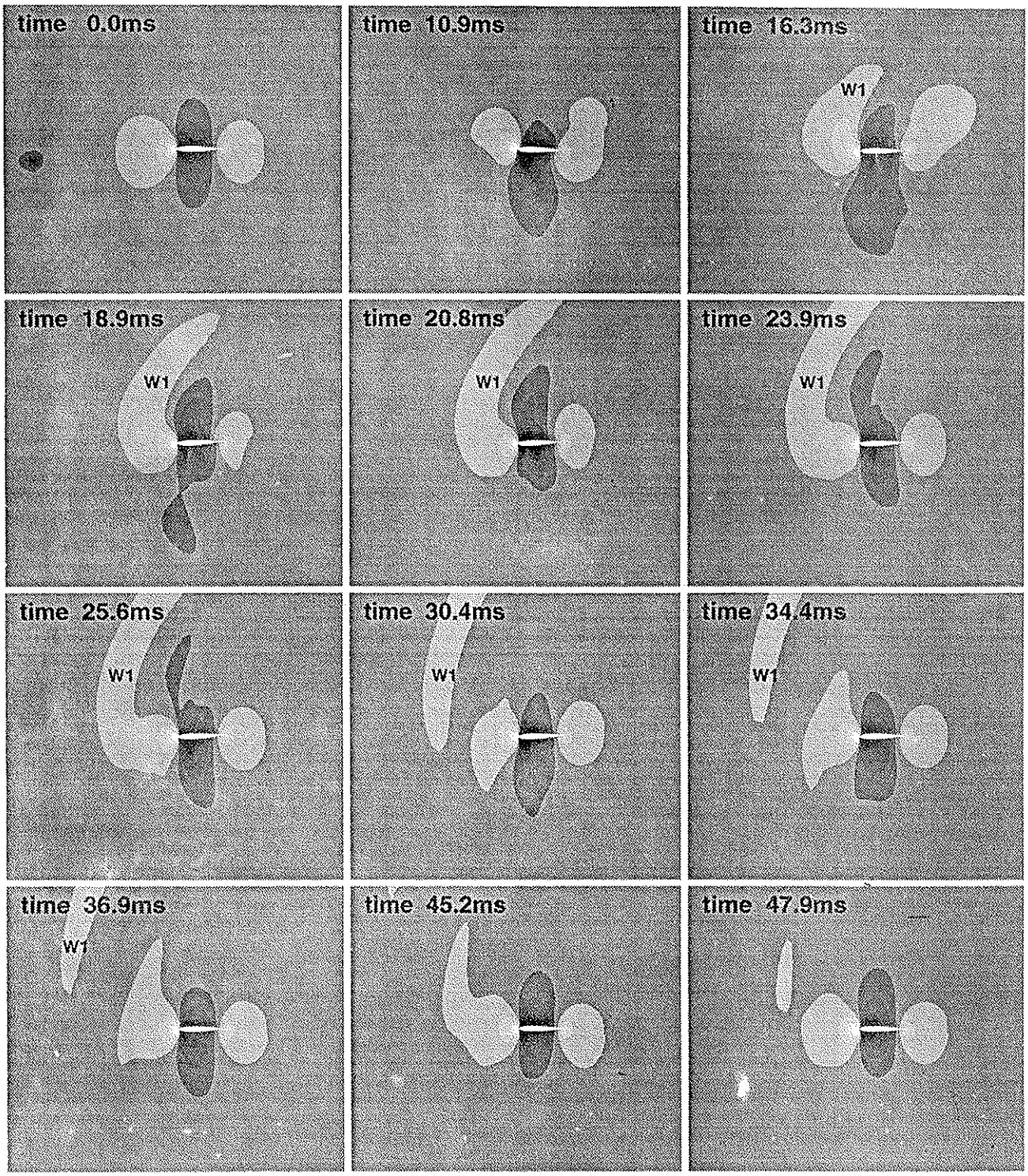

Figure 20: Pressure contours for a sequence of time steps during BVI for the IBC-case ($M_\infty = 0.73$, $\Gamma = 0.4$, $z_v = -0.26$, NACA0012)

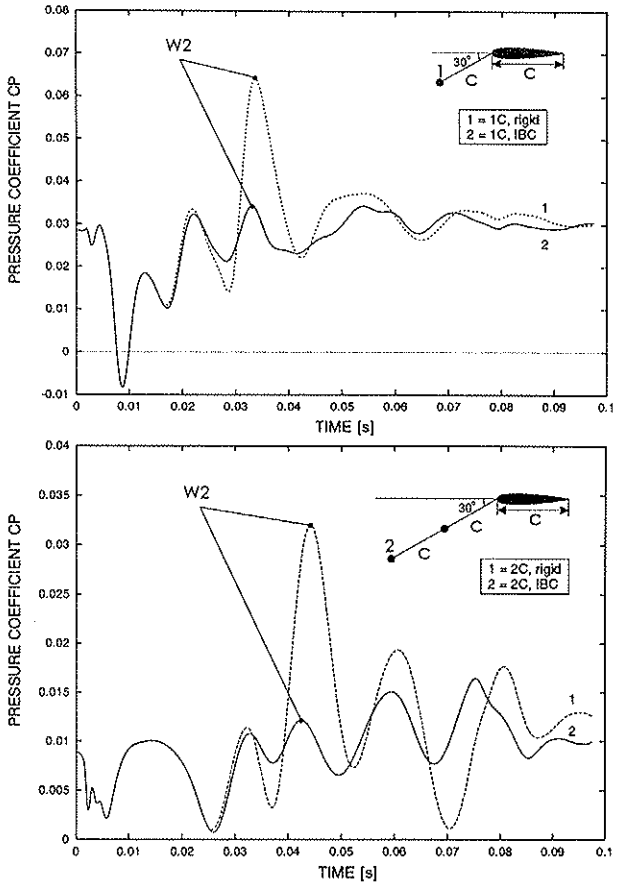

Figure 21: Time history of the pressure coefficient at two observer points below the airfoil for the rigid (dotted curve) and the IBC-case (solid curve). $M_\infty = 0.73$, $\Gamma = 0.4$, $z_v = -0.26$, NACA0012

refore research has been concentrated on detecting appropriate active control movements of the rotor–blade segment: the time history of a BVI–noise diminishing pitching control motion (IBC) has been determined and is discussed in detail. Since the results are very promising, further computations will be performed focussing on the pitch horn movement that generates the desired pitching control motion at the tip region of the elastic rotor–blade where the BVI is most intense. Due to tho rotor–blades's torsional wave speed, its elasticity has to be taken into account and leads to a significant time lag between the pich horn motion at the rotor–blade's root and the motion at the tip region. Furthermore the pitch horn motion differs from the motion at the tip region because of dispersion. The computer code ODISA will be used for the structural analysis. A short validation of ODISA is included.

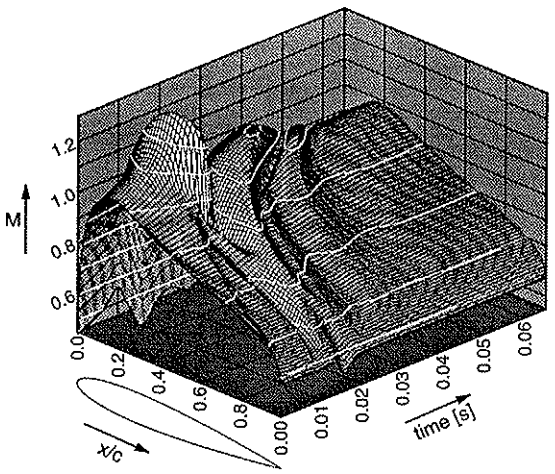

Figure 22: Mach number at lower side during BVI for the IBC-case ($M_\infty = 0.73$, $\Gamma = 0.4$, $z_v = -0.26$, NACA0012)

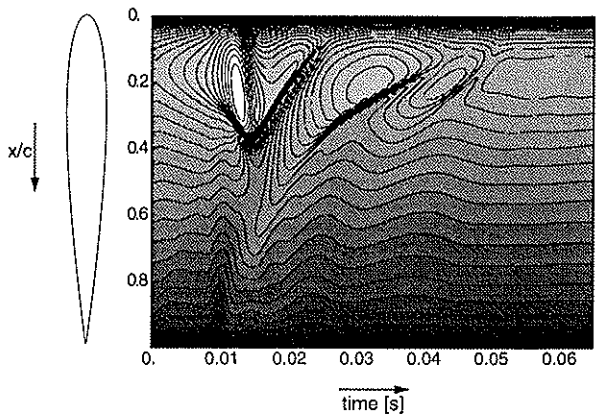

Figure 23: Isolines of the history of the Mach number at lower side during BVI for the IBC-case ($M_\infty = 0.73$, $\Gamma = 0.4$, $z_v = -0.26$, NACA0012)

6 Acknowledgements

This work was supported by the Deutsche Forschungsgemeinschaft whose assistance is gratefully acknowledged. We would like to thank Dr. A. Brenneis and Dr. A. Eberle from DASA for providing the computer code INFLEX. Computations were performed using the facilities of the Rechenzentrum der RWTH Aachen.

References

[1] G.E.A. Meier and R. Timm, Unsteady Vortex Airfoil Interaction, AGARD CP-386, 1985, 16.1-16.10

[2] G.E.A. Meier, U. Schievelbusch, H.-M. Lent, Stoßwellenentstehung bei transsonischer Wirbel–Profil–Wechselwirkung, ZFW 14, 1990, pp. 327-332

[3] H.M. Lent, G.E.A. Meier, K.J. Müller, F. Obermeier, U. Schievelbusch and O. Schürmann. Mechanisms of transonic Blade-Vortex Interaction Noise. Journal of Aircraft, Vol. 30, No. 1, 1993, pp. 88-93

[4] F.X. Caradonna, R.C. Strawn and J.O. Bridgeman, An Experimental and Computational Study of Rotor-Vortex Interactions, 14th European Rotorcraft Forum, 1988

[5] C. Kitaplioglu, F.X. Caradonna, Aerodynamics and Acoustics of Blade-Vortex Interaction Using an independently Generated Vortex, American Helicopter Society Aeromechanics Specialists Conference, San Francisco, 1994

[6] D. Bershader, Shock Tube Studies of Vortex Structure and Behaviour, in: H. Grönig (Ed.), Proc. of the 16th Int. Sym. on Shock Tubes and Waves, Aachen, July 1987, Weinheim, VCH, 1988

[7] S. Lee, D. Bershader, Head-On Parallel Blade-Vortex Interaction, AIAA Journal, Vol. 32, No.1, 1994, pp.16-22

[8] M.H. Horner, E. Saliveros and R.A. Mc. D. Galbraith, An Experimental Investigation of the Oblique Blade-Vortex Interaction, 17th European Rotorcraft and Lift Aircraft Forum, Berlin, Germany, Sept. 1991

[9] B.G. von der Wall, BVI visualisation and correlation with sectional airloads, ZFW 19, 1995, pp. 261-266

[10] H.E. Jones and F.X. Caradonna, Full-Potential Modelling of Blade-Vortex Interactions, 12th European Rotorcraft Forum, Paper No. 27, 1986

[11] K. Ramachandran, S. Schlechtriem, F.X. Caradonna, J. Steinhoff, The Application of Vorticity Embedding to the Computation of Advancing Rotor Flows, presented at the 49th AHS Annual Forum, St. Louis, MO, 1993

[12] K. Ramachandran, S. Schlechtriem, F.X. Caradonna, J. Steinhoff, Free-Wake Computation of Helicopter Rotor Flowfields in Forward Flight, AIAA - 93 - 3079, 1993

[13] G.R. Srinivasan, W.J. McCroskey and J.D. Baeder, Aerodynamics of Two-Dimensional Blade-Vortex Interaction, AIAA-Journal, Vol. 24, No. 10, Oct. 1986

[14] J. Ballmann and C. S. Kocaaydin, Some Aerodynamic Mechanisms of Impulsive Noise during Blade-Vortex-Interaction, 16th European Rotorcraft Forum, 1990, pp. II.10.1.1-II10.1.14

[15] D. Nellessen, S. Schlechtriem, J. Ballmann, *Elastic Deformation Of Rotor–Blades Due To BVI,* Proceedings of the 19th European Rotorcraft Forum, Paper No. B1, 1993

[16] D. Nellessen, S. Schlechtriem, J. Ballmann, *The Impact of Blade Vortex Interaction on the Elastic Deformation of Wings,* presented at the Euromech Colloquium 300, Interaction between vorticity fields and boundaries, Istanbul, 1993

[17] S. Schlechtriem, D. Nellessen, J. Ballmann, *A Numerical Investigation of the Influence of Active Control Movements on Vibration and BVI–Noise,* Proceedings of the 20th European Rotorcraft Forum, Paper No. 100, 1994

[18] S. Körber and J. Ballmann, Mechanisms and Acoustics of Blade–Vortex–Interactions, ZFW 19, 1995, pp. 397-406

[19] F.H. Schmitz, *Rotor noise,* Aeroacoustics of Flight Vehicles, I: Noise Sources; Ed. H.H. Hubbard, publ. ASA/AIP, 1995, pp. 65-149

[20] W.R. Splettstoesser, K.-J. Schultz, R. Kube, T.F. Brooks, E.R. Booth, G. Niesl and O. Streby, BVI Impulsive Noise Reduction By Higher Harmonic Pitch Control: Results Of A Scaled Model Rotor Experiment In The DNW, 17th European Rotorcraft Forum, 1991

[21] P. Richter and H.D. Elsbrechter, Design and First Tests of Individual Blade Control Actuators , 16th European Rotorcraft Forum, 1990

[22] S. Schlechtriem, D. Nellessen, S. Brinker, G. Britten and J. Ballmann, Prediction of Rotor-Blade Deformations Due to Unsteady Airloads, Final Technical Report ERO, Contract N 6817194 C 9098, 1995

[23] D. Nellessen, Schallnahe Strömungen um elastische Tragflügel, Dissertation, Rheinisch–Westfälische Technische Hochschule Aachen, Mathematisch–Naturwissenschaftliche Fakultät, 1995

[24] A. Brenneis and A. Eberle, Application of an Implicit Relaxation Method Solving the Euler Equations for Time-Accurate Unsteady Problems, Journal of Fluids Engineering, Vol. 112, Dec 1990, pp 510-520

[25] A. Brenneis and A. Eberle, Evaluation of an Implicit Euler Code Against Two and Three-Dimensional Standard Configurations, in: AGARD CP-507: Transonic Unsteady Aerodynamics and Aeroelasticity, Paper No. 10, March 1992

[26] M. Botz, P. Hagedorn, On the Dynamics of Multibody Systems with Elastic Beams, Advanced Multibody System Dynamics pp. 217-236, Kluwer Academic Publisher, Netherlands, 1993

[27] A.R.S. Bramwell, Helicopter Dynamics, Arnold, London, 1976

[28] K. Washizu, Variational Methods in Elasicity and Plasticity, second edition, Pergamon Press, 1975

[29] T. J. R. Hughes, The Finite Element Method, Prentice- Hall Inc., Englewood Cliffs New Jersey, 1987

[30] Sharpe D.L.," An Experimental Investigation of the Flap-Lag-Torsion Aeroelastic Stability of a Small-Scale Hingeless Helicopter Rotor in Hover," NASA Technical Paper 2546, AVSCOM Technical Report 85-A-9, 1986